

Earthquake record truncation metric for nonlinear dynamic analyses of high rockfill dams

Qiuting Jiang^{a,b}, Degao Zou^{a,b,*}, Jingmao Liu^{a,b}, Yongqian Qu^{a,b}, Kai Chen^{a,b},
Chenguang Zhou^{a,b}, Duo Li^{a,b}

^a The State Key Laboratory of Coastal and Offshore Engineering, Dalian University of Technology, Dalian, Liaoning 116024, China

^b School of Hydraulic Engineering, Dalian University of Technology, Dalian, Liaoning 116024, China

ARTICLE INFO

Keywords:

High rockfill dam
Seismic duration
Crest settlement
Horizontal displacement
Probability

ABSTRACT

The long initial and coda waves with small amplitude are often observed in an actual earthquake record. Truncating those wavebands that contribute little to structural responses is helpful to focus on the strong shaking phase and reduce computational cost. In the paper, 157 actual earthquake records and the acceleration time windows constrained by truncation thresholds of Arias intensity serve as input ground motions. A large number of elastoplastic dynamic analyses on a 295 m-high core-wall rockfill dam (CRFD) are conducted using the generalized plasticity model and seismic wave input method. Inspired by fragility equation, the probability curves for the accuracy loss of dam response less than different limits under different truncation thresholds are established, quantifying the destructiveness of the truncated seismic acceleration time windows. Results show that the probabilities are minimally affected by peak ground acceleration (PGA); the allowable tail truncation of earthquake records is much more than the leading due to the asymmetry of seismic waveforms and the cyclic hardening characteristic of rockfill materials; the truncation metric of 0.01–98 % Arias intensity is proved to be effective and robust in accelerating dynamic analyses of rockfill dams with an accuracy loss within 5 % and an average reduction in computational workload of approximately 50 %.

1. Introduction

In recent years, a large number of high rockfill dams have been built, under construction, and planned. With the increase of global crustal activity trends, seismic damage prediction of high rockfill dams and post-earthquake performance emergency assessment are of increasing interest [1–6]. The time-domain step-by-step integration method is commonly adopted in dynamic analyses of rockfill dams [7–9], which requires solving structural dynamic equilibrium equations at each time step. The longer the earthquake record, the greater the computational workload. Meanwhile, the number of elements, nodes and degrees of freedom in finite element model sharply increases with the increase of dam height. When the sample size is large, the computational cost becomes too burdensome for regular workstations to handle.

During seismic wave propagation, the coda wave at an earthquake record tail suffers pronounced attenuation due to the late arrivals of the scattering and diffracted waves that travel along longer and indirect

paths [10–12]. Furthermore, during data collection, in addition to recording signals excited by various target sources, seismographs also capture a multitude of noises from the instruments and the surrounding environment [11,13]. Earthquake data processing and cataloging (for example, initial arrival picking, etc.) inevitably are affected by these noises. Therefore, a gentle start and a long tail are always observed in an actual earthquake record. These wavebands usually have a weak acceleration amplitude and their contribution to structural damage may be negligible. However, they also need occupy a large amount of computational time and resources in finite element numerical calculations. Removing these wavebands may be effective in reducing the workload of data storage, analysis, and simulation.

In the last decades, more than 30 metrics have been defined in literature to identify and extract the strong shaking phases of earthquake records from acceleration and energy viewpoints [14]. These definitions are mainly divided into three groups: bracket duration, uniform duration, and significant duration [14]. The bracket duration is defined as

* Corresponding author at: The State Key Laboratory of Coastal and Offshore Engineering, Dalian University of Technology, Dalian, Liaoning 116024, China.

E-mail addresses: dagongshujqt@mail.dlut.edu.cn (Q. Jiang), zoudegao@dlut.edu.cn (D. Zou), liujm@dlut.edu.cn (J. Liu), quyongqian@dlut.edu.cn (Y. Qu), chenkai@dlut.edu.cn (K. Chen), zhchg@dlut.edu.cn (C. Zhou), liduo1226@163.com (D. Li).

<https://doi.org/10.1016/j.istruc.2024.107913>

Received 15 August 2024; Received in revised form 28 October 2024; Accepted 22 November 2024

Available online 4 December 2024

2352-0124/© 2024 Institution of Structural Engineers. Published by Elsevier Ltd. All rights are reserved, including those for text and data mining, AI training, and similar technologies.

the time window between the first and last excursions of a specified earthquake acceleration threshold. The uniform duration is defined as the sum of the time intervals of all excursions of a specified acceleration threshold, and is not a continuous time window. The duration for an earthquake under different PGA levels does not remain constant when using these two definitions and may even be zero at a large threshold. The significant duration refers to the time window constrained by two fractions AI_0 and AI_f (unit: %) of Arias intensity [15–17]. Arias intensity is defined as the integral of the square of seismic acceleration over total duration, and its accumulation process describes the accumulation and attenuation of earthquake energy [14,18]. Therefore, the group is extensively used for different purposes [19,20], especially the significant durations of 5–95 % Arias intensity [12] and of 5–75 % Arias intensity [21]. However, these truncation thresholds seem to be determined purely based on visual inspection of earthquake records.

Recently, many scholars have proposed the earthquake record truncation methods incorporating structural characteristics in order to improve the computational efficiency of structural dynamic analyses. Repapis et al. (2020) [22] and Dimakopoulou et al. (2022) [23] applied a pulse duration constrained by the predominant velocity pulse of near-field directivity records to dynamic analyses of RC buildings. Jin et al. (2020) [24] proposed an acceleration response spectrum-based earthquake record truncation method for nonlinear dynamic analyses of arch dams. Reyes et al. (2021) [25] suggested the truncation thresholds of 10 % and 20 % peak roof displacement of an equivalent SDOF system to trim the leading and trailing weak signals of earthquake records. Li et al. (2022) [7] identified the truncation points of earthquake records using the maximum displacement response of equivalent SDOF systems and applied the truncated records to maximum displacement response analyses of MDOF structures. He et al. (2024) [9] used neural networks to predict the truncation point as an alternative to time-history analyses on SDOF in Li et al. (2022). However, most of these studies focus on SDOF and RC frame structures and the operation of the record truncation methods proposed is somewhat complex. It is not applicable for high rockfill dams with large volume and complex behavior.

2. Aim of the study

This paper aims to identify the effective seismic time window for high rockfill dams by trimming the low-amplitude initial and coda waves of earthquake records. The significant duration definition is used as the truncation method for earthquake records. A total of 157 actual earthquake records from PEER NGA database and the seismic acceleration time windows extracted using different truncation thresholds of Arias intensity are used as input ground motions. A large number of nonlinear dynamic analyses on a 295m-high CRFD are conducted. In these analyses, the generalized plasticity model is used to simulate the cyclic hysteretic characteristics and cumulative residual deformation of rockfill materials. The seismic wave input method is used to simulate the dynamic interaction between dam and bedrock and the radiation damping of infinite canyon. Ground motion duration is used as intensity measure (IM), and the accuracy loss of crest settlement caused by record truncation is used as structural damage parameter (EDP). Based on the extension of fragility function, the probability curves of EDP less than different limits under different IM levels (equivalently, different truncation thresholds) are obtained using Monte Carlo Simulation and maximum likelihood method. Thus, the destructiveness of the seismic acceleration time windows extracted by different truncation thresholds can be quantified in terms of structural response. Finally, the optimal earthquake record truncation metric proposed is tested from dam horizontal displacements and response spectra.

3. Probabilistic seismic analysis method

Fragility analysis is an essential component of probabilistic seismic analysis and enables to predict the likelihood of structures reaching

different damage states at various levels of ground motion intensity measure (IM). The fragility function is typically expressed as the exceedance probability of structural damage state y at a specified ground motion intensity level im . The IM that causes the structure to reach y is often assumed to follow a lognormal distribution [26], as shown in Eq. (1). It requires that the EDP and IM be positively correlated. In previous probability analyses, peak ground acceleration PGA and seismic acceleration response spectrum S_a are always used as IM [26–28].

$$P_R(y|IM = im) = P_{EDP|IM}(EDP > y|IM = im) = P_{IM|EDP}(IM \leq im|EDP = y) = \Phi\left(\frac{\ln im - \theta}{\sigma}\right) \quad (1)$$

And the conditional probability that the EDP is below the damage state y at the ground motion intensity level im is:

$$P_{EDP|IM}(EDP \leq y|IM = im) = 1 - \Phi\left(\frac{\ln im - \theta}{\sigma}\right) \quad (2)$$

in which $\Phi()$ represents the standard normal distribution function; θ and σ are the log-mean and log-standard deviation, respectively.

When EDP is negatively correlated with IM , the conditional probability that the EDP is below the damage state y at the ground motion intensity level im should be expressed as:

$$P_{EDP|IM}(EDP \leq y|IM = im) = P_{IM|EDP}(IM \leq im|EDP = y) = \Phi\left(\frac{\ln im - \theta}{\sigma}\right) \quad (3)$$

The lognormal distribution parameters θ and σ can be determined through the multiple-stripe analysis (MSA) method and maximum likelihood method (MLE) [26]. The calculation starts by scaling a suite of earthquake records to multiple target IM levels. Then, using these scaled records as ground motion input, a series of structural nonlinear dynamic analyses are performed to obtain the EDP values. The resulting plot of $EDPs$ at an IM level looks like a “stripe” and hence multiple stripes of data at these target IM levels can be obtained. The fractions of records that cause the structure reaching a given limit state at each stripe are counted and then the parameters θ and σ at the limit state can be obtained using the MLE method. Finally, the lognormal distribution can be fitted. In this paper, ground motion duration is used as the IM (see Section 4.3); the accuracy loss of structural response caused by earthquake record truncation is used as the EDP (see Section 4.4).

4. Computational model

4.1. Finite element model

In this paper, a 295 m high CRFD is adopted as the benchmark. The crest width is 16 m, and the upstream and downstream slopes of the dam are 1:2.0 and 1:1.9, respectively. There are seven material zones in total, including cofferdam, rockfill I, II and III zones, transition, filter and core wall. The dam construction is completed in 49 layers. The reservoir is filled in 47 steps to the height of 285 m. The bedrock foundation truncated from the infinite canyon is 2414 m long and 531 m deep [29]. Given the large geometric span of different material zones, the finite element model including 18258 elements and 18506 nodes is established using the quadtree technique (see Ooi et al. (2015) [30] for details), as shown in Fig. 1. This technique enables fast and high-quality automatic mesh discretization and adaptive mesh refinement [30]. Two element types, the isoparametric element and the scaled boundary finite element [31,32], are employed in the model. Referring to existing researches [3,6,33], the element sizes of bedrock and rockfill zones are set to be 12 m and 6 m, respectively, and the central core wall and filter are finely discretized with a mesh size of 3 m. The element size spanning in the transition zone is accomplished using polygonal elements generated by the scaled boundary finite element method. The nonlinear

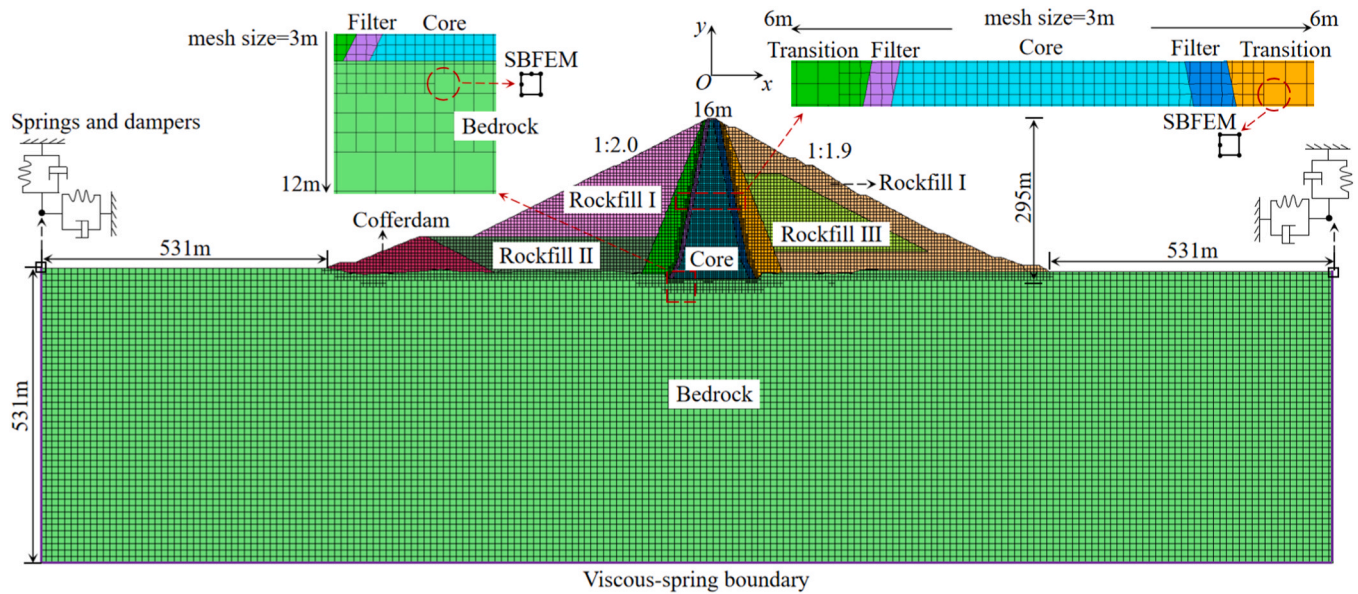


Fig. 1. Finite element model of the dam.

dynamic analyses of the dam are carried out based on the stress state provided by static analysis. In dynamic calculations, the added mass method [34] is employed to simulate the hydrodynamic pressure. The nonlinear finite element analysis program GEODYNA [35], developed by Earthquake Engineering Research Institute, Dalian University of Technology, is used.

4.2. Constitutive model and material parameters

Many researches [14,19] indicated that ground motion duration has a significant effect on structural elastoplastic response and cumulative hysteretic energy dissipation. Therefore, the generalized plasticity model modified by Zou et al. [37] is adopted here (see Appendix B). This model is fairly equipped to simulate nonlinear behaviors of geotechnical structures for the following reasons: (a) the plastic flow direction, loading direction and plastic modulus of rockfills are directly determined instead of the plastic potential surface and yield surface; (b) the dilation and contraction, pressure dependence, cyclic cumulative residual deformation and cyclic hysteresis behaviors of rockfills are taken into account; (c) the structural static and dynamic analyses are allowed to be completed using a suite of model parameters. This model has been successfully applied in many research studies and actual engineering [36,37]. The dam material parameters used in this paper are shown in Table 1. For simplification, the same parameters are used for all dam shell materials. The bedrock is simulated using the linear elastic model, with elastic modulus $E = 20$ GPa, density $\rho = 2450$ kg/m³, and Poisson's ratio $\nu = 0.25$.

4.3. Ground motion records and intensity measure (IM)

The NGA database [38] of Pacific Earthquake Engineering Research Center (PEER, <https://peer.berkeley.edu/>) has collected a vast array of earthquake records in active tectonic regimes. The database possesses the most comprehensive set of metadata, including time series, response spectra, peak ground acceleration (PGA), duration, etc. These

earthquake records and metadata have been subjected to multiple quality checks, including the sufficient signal-to-noise ratio and the instrument parameters (for example, anti-alias filter corner, etc.) and the baseline errors (e.g., excluding baseline errors with multiple jumps or time-related trends) [38]. Therefore, 157 earthquake records with PGA greater than 0.2 g, length ranging from 10 s to 160 s, and magnitude ranging from 5.0 to 7.9 are selected and used here from the database. Fig. 2(a) and (b) show the distributions of length and PGA of these records, respectively. Appendix Table A.1 summarizes the records used in this study, mainly from 19 earthquake events such as CHI-CHI, Coalinga, Kobe, etc.

Ground motion duration is used as the IM. The seismic acceleration time windows constrained by different truncation thresholds of Arias intensity are used as input ground motions. The Arias intensity is denoted as AI , as shown in Eq. (4), and the significant duration is denoted as $D_{a-b\%AI}$, where a and b mark the beginning and end of the truncated time window, respectively. Based on previous studies [12,14,21], the value of a is taken as 0, 0.01, 0.1, 1, 3, 5, respectively; the value of b is taken as 80, 83, 85, 88, 90, 93, 95, 98, 100, respectively. As the truncation threshold varies, the length of the input ground motion is "scaled" to different IM levels. At a specified IM level, the PGA of input ground motions is adjusted to the same level and is amplified to 0.3 g, 0.5 g, and 0.8 g, respectively. The amplification factors of 2–4 times for ground motion acceleration have been proven to be acceptable [39]. In dynamic calculations, the ground motions are input in the stream direction into the dam-bedrock system through seismic wave input method (see Section 5).

$$AI = \frac{\pi}{2g} \int_0^T (a(t))^2 dt \quad (4)$$

in which AI is the Arias intensity of an earthquake record; T is the length of the record; $a(t)$ is the seismic acceleration time history; g is the acceleration due to gravity.

Table 1

The generalized plasticity model parameters of dam materials.

symbol	G_0	K_0	m_s	m_v	M_g	M_f	α_f	α_g	H_0	m_l	β_0	β_1	H_{u0}	m_u	r_d	γ_{DM}	γ_u
dam shell	1200	1400	0.5	0.5	1.77	0.99	0.45	0.50	900	0.40	24	0.045	3000	0.50	100	50	5
core wall	800	1000	0.3	0.3	1.25	1.21	0.01	0.01	430	0.15	35	0.001	800	0.15	100	60	1

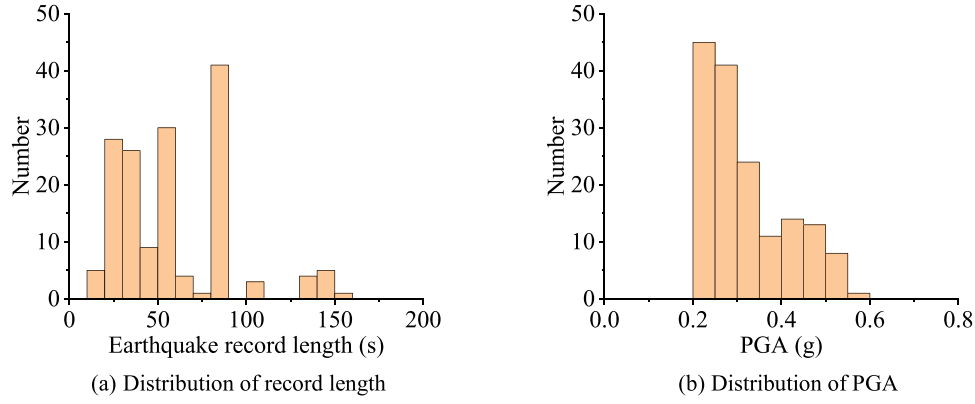


Fig. 2. Actual earthquake records.

4.4. Structural damage parameter (EDP)

The crest settlement is the most representative and commonly used indicator to assess the damage of rockfill dams [40–45]. The relative difference ΔS between the crest settlements under an original earthquake record and the seismic acceleration time window extracted using $D_{a-b\%AI}$ is used here as the EDP, as Eq. (5). The value of ΔS represents the destructiveness loss before and after truncating the earthquake record and the computational accuracy loss of dam damage. A small value of ΔS indicates a minor loss of accuracy. Thus, six limits for ΔS are suggested, i.e., 5 %, 10 %, 15 %, 20 %, 25 %, and 30 %.

$$\Delta S = \frac{|S_0 - S_{IM}|}{S_0} \quad (5)$$

where S_0 is the crest settlement under an original earthquake record; S_{IM} is the crest settlement under the seismic acceleration time window extracted using $D_{a-b\%AI}$.

5. Ground motion input

5.1. Seismic wave input method

Actually, the structure-foundation system is an energy-open system, and the interaction between structure and foundation induces a significant impact on structural responses [28,46,47]. For simplification, ground motion input is generally implemented using uniform excitation method in traditional structural dynamic analyses [48]. In the method, the massless foundation input model [47,49] is used, in which the elastic massless foundation with fixed constrained boundaries is assumed. In calculation, the free-field acceleration time history is uniformly applied at the foundation [47]. This method neglects the spatial variation of ground motion input due to large size and span of structures (like dams, bridges), wave passage effect, site effect, and topographic effect, resulting in the distortion of numerical results [48,50].

To estimate structural dynamic responses accurately, seismic wave input method (i.e., non-uniform excitation method) is applied here. In the method, the interaction between structure and foundation and the radiation damping of infinite canyon are simulated by adding viscous-spring boundaries and equivalent loads on the truncated interfaces of foundation [46,47,51]. The viscous-spring boundary [52,53] is implemented by installing pairs of spring and viscous damper on the truncated interfaces of foundation. Normal and tangential spring-damper pairs are installed at each node of the truncated interfaces to simulate the elastic recovery mechanism of foundation and the radiation effects of far-field rock, as shown in Fig. 1. Simultaneously, ground motions are input as equivalent nodal forces exerted on the truncated boundaries. The equivalent nodal forces satisfy the displacement and stress conditions due to the free field on the truncated boundaries of foundation and can

be obtained from Eq. (6).

$$\mathbf{F}_b = \mathbf{R}_b^{\text{ef}} + \mathbf{C}_b \dot{\mathbf{u}}_b^{\text{ef}} + \mathbf{K}_b \mathbf{u}_b^{\text{ef}} \quad (6)$$

where \mathbf{u}_b^{ef} , $\dot{\mathbf{u}}_b^{\text{ef}}$ and \mathbf{R}_b^{ef} are the displacement vector, velocity vector and the corresponding force vector at the bedrock boundary nodes induced by the free field, respectively. \mathbf{K}_b and \mathbf{C}_b are the additional stiffness matrix and damping matrix of the viscous-spring boundary, respectively.

5.2. Example verification

Herein, the feasibility and reliability of the seismic wave input method are demonstrated by a symmetrical V-shaped canyon problem. The finite element model of the half-space truncated from an infinite canyon has a width of 6000 m and a depth of 2000 m, as shown in Fig. 3, and the mesh size is less than 1/10 of the wavelength of incident wave [54]. The V-shaped canyon, whose half-width $w = 1000$ m and depth $d = 1000$ m, is embedded in the half-space. The wave medium has a density $\rho = 2670$ kg/m³, shear wave velocity $v_s = 1000$ m/s, and Poisson's ratio $\nu = 1/3$. The unit-amplitude SH wave with circular frequency $\omega = \pi$ rad/s and displacement in the z -direction is incident from the bottom of the model and the incident angle α of 0° and 45° are considered, respectively.

The finite element results for the surface displacement amplitudes are compared with the analytical solutions of Gao et al. (2013) [50]. Fig. 4 plots the normalized displacement amplitudes along the horizontal ground surface and the canyon surface against the horizontal x -axis. The $|u_z|/|u_f|$ represents the steady-state surface displacement amplitude $|u_z|$ of the half-space normalized by the free field amplitude $|u_f|$. It can be seen that the numerical solutions match well with the analytical solutions.

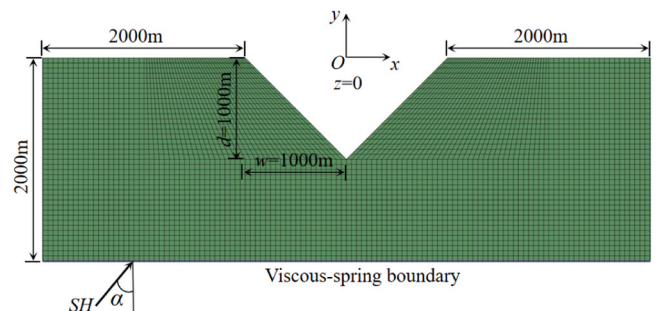


Fig. 3. Finite element model of V-shaped canyon.

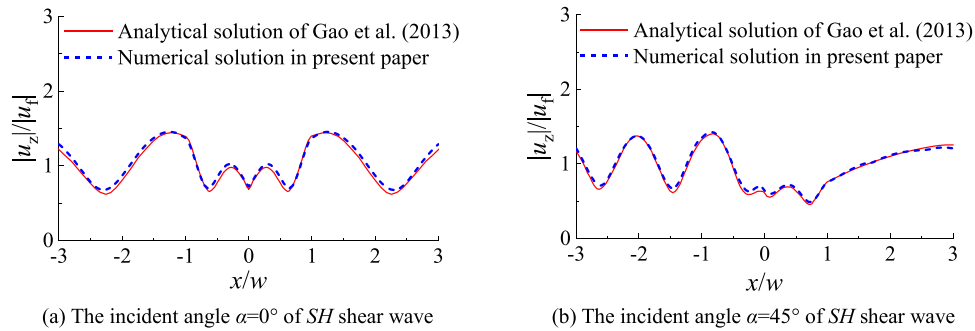


Fig. 4. Distribution of normalized surface displacement amplitude for the half-space along the x-axis.

6. Analyses and discussions

6.1. Crest settlement

Swaisgood (2003) [55] conducted an extensive survey on seismic damage of rockfill dams worldwide, providing a rough distribution of crest settlement ratios (crest settlement/dam height) under different PGA levels. The survey serves as a valuable reference for numerical simulations of similar engineering. Fig. 5 presents the distributions of crest settlement ratios of the benchmark dam in this paper under 157 original earthquake records for PGA = 0.3 g, 0.5 g, and 0.8 g. It can be seen that the simulated crest settlement ratios range from 0.03 % to 1 %, which is consistent with engineering experience.

Fig. 6 shows the crest settlement time histories calculated under two typical earthquake records (stations CHY006-N and LDM334). It can be seen that the evolution rules of the crest settlements are consistent with the growth and decay patterns of the seismic acceleration time histories. The central strong shaking phases induce a rapid growth of crest settlements, while the settlements tend to be horizontal at the beginning and end of the records. It is worth noting that the earthquake record at station CHY006-N is much longer than that at station LDM334, whereas the crest settlement calculated under CHY006-N is less than that under LDM334 for the same PGA level. It indicates that the evolution of structural damage can't be quantified by single ground motion parameter. Later, we will identify the seismic time window that contributes significantly to dam damage from the perspective of earthquake energy.

6.2. Probability analyses

This part seeks to identify an optimal truncation metric for initial and tail waves of earthquake records and then the truncated seismic time windows can be used to accelerate dynamic analyses of rockfill dams at a minor accuracy loss.

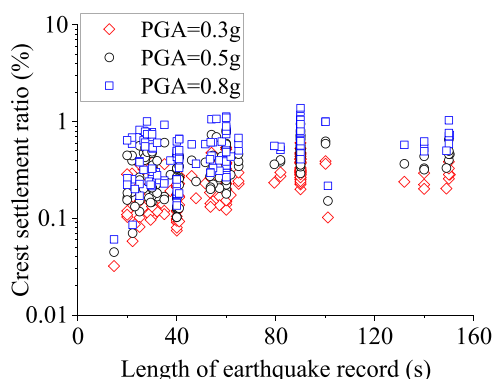


Fig. 5. Crest settlement ratio of the dam under 157 earthquake records.

6.2.1. Discussion on the b value in $D_{a-b\%AI}$

In this section, the value of a is set to be 0, and the value of b is taken as 80, 83, 85, 88, 90, 93, 95, 98, 100, respectively. The seismic acceleration time windows extracted by $D_{0-b\%AI}$ are applied to the benchmark dam to obtain crest settlements through nonlinear dynamic analyses. The accuracy loss of crest settlements, ΔS , is calculated using Eq. (5), and then the stripe plots of $D_{0-b\%AI}-\Delta S$ are obtained. 157 numerical calculations have been performed for each horizontal stripe of $D_{0-b\%AI}-\Delta S$. As shown in Fig. 7, the resulting $D_{0-b\%AI}-\Delta S$ plots under PGA = 0.3 g, 0.5 g and 0.8 g are given in hollow dots with different colors, and the mean of ΔS at each stripe is presented in solid dots. The counted fractions of records that cause ΔS less than different limits at each stripe are plotted in hollow dots in Fig. 8. It can be seen that the variation of PGA induces little influence on the fractions although some difference in the distributions of ΔS .

Fig. 9 provides some statistics of truncation of 157 earthquake records under $D_{0-b\%AI}$ and duration of the extracted seismic time windows (PGA=0.3 g). Obviously, a small b value induces a large truncation for an earthquake record and further a high ΔS . Therefore, the Eq. (3) is used to fit the lognormal distribution and the corresponding parameters of θ and σ at each limit are estimated using MLE method, as shown in Table 2. Then, the probability curves for ΔS less than those limits are obtained, as shown in Fig. 8. The probabilities for the limits of 20 %, 25 %, and 30 % are provided as references and not discussed in detail. From these curves, the probability for ΔS less than a specified limit increases as the value of b increases. It can be found that the value of b should be at least greater than 98 to yield an accuracy loss within 5 %. When the truncation threshold $b=98$, the probability of ΔS less than 5 % reaches 88.48 %, less than 10 % reaches 92.12 %, and less than 15 % reaches 93.82 %, demonstrating the robustness of the truncation metric. From Fig. 9, the average truncation of earthquake records reaches about 45 % (the maximum reaches 90 %) under $D_{0-98\%AI}$, and the average duration of the extracted seismic acceleration time windows is about 35 s. It indicates that trimming the coda waves of earthquake records using $D_{0-98\%AI}$ has little effect on the estimation of EDP but is effective in reducing computational effort.

6.2.2. Discussion on the value of a in $D_{a-b\%AI}$

Based on the above analysis, different values of a in $D_{a-b\%AI}$ are discussed in this section while the value of b is set to be 98. The value of a is taken as 0, 0.01, 0.1, 1, 3, 5, respectively. Similarly, the stripe plots of $D_{a-98\%AI}-\Delta S$ under PGA = 0.3 g, 0.5 g, and 0.8 g are obtained by applying the seismic acceleration time windows extracted by $D_{a-98\%AI}$ into dynamic analyses on the benchmark dam, as shown in Fig. 10. The counted fractions of records that cause ΔS less than different limits at each stripe are plotted in Fig. 11. Among them, the fractions for the limits of 20 %, 25 % and 30 % approach 100 % and are not given here. It can be seen that the fractions are also not sensitive to the variation of PGA.

Similarly, Fig. 12 provides some statistics of truncation of 157 earthquake records under $D_{a-98\%AI}$ and duration of the extracted seismic

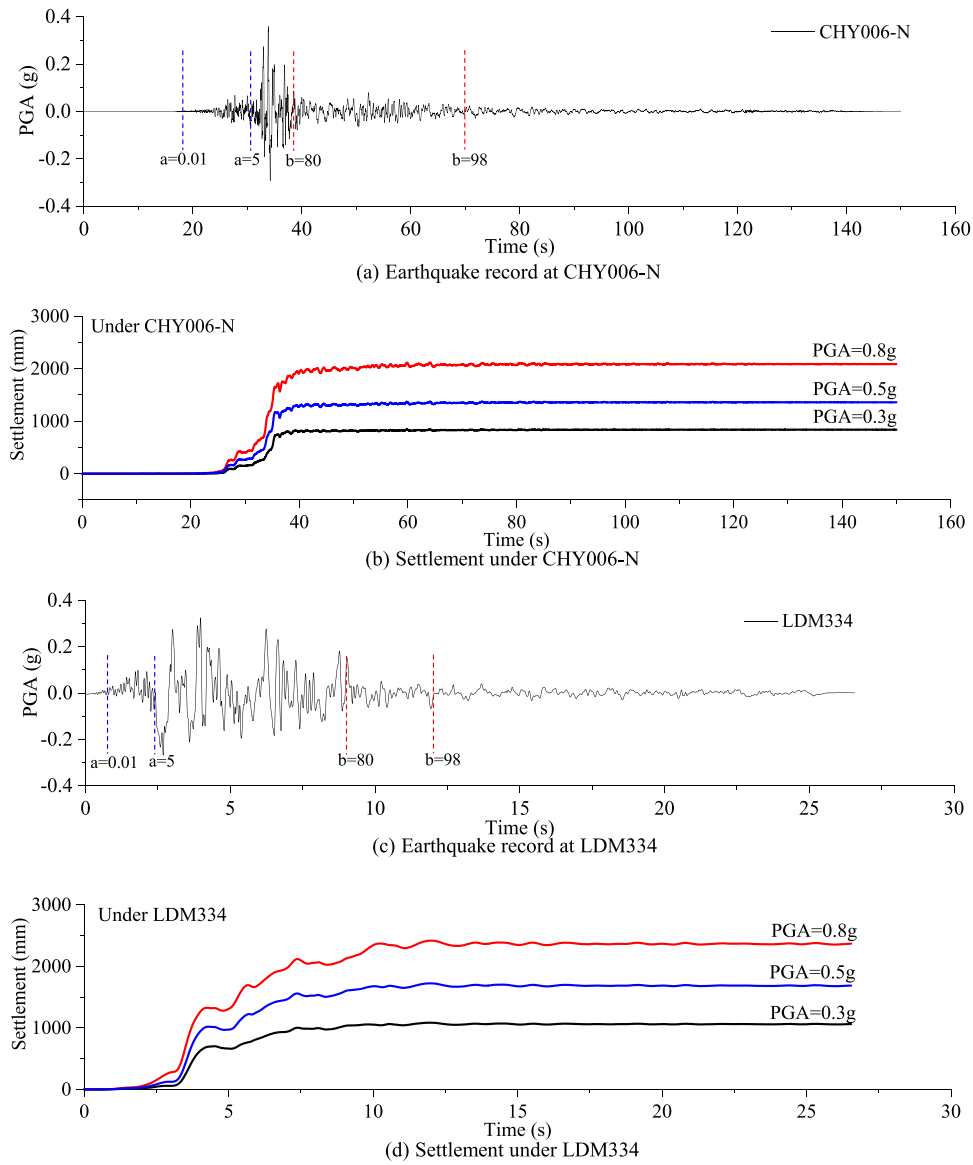
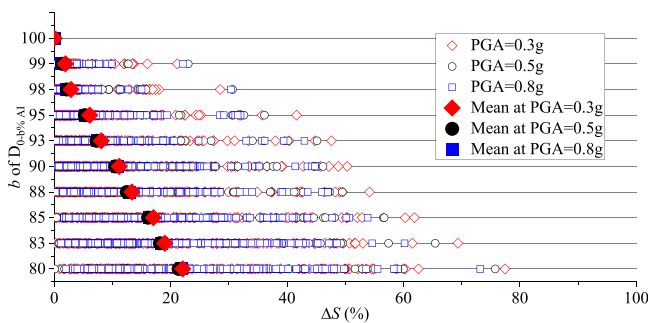


Fig. 6. Settlement time histories of dam crest.

Fig. 7. $D_{0-b\%AI}-\Delta S$ stripe plots.

time windows (PGA=0.3 g). Obviously, a large a value induces a large ΔS (because the truncation for a record is large). Therefore, the Eq. (2) is used to fit the lognormal distribution and the corresponding parameters of θ and σ at each limit are estimated using MLE method, as shown in Table 3. The probability curves for ΔS less than those limits are shown in Fig. 11. From these curves, the probability for ΔS less than a specified

limit decreases as the value of a increases. The value of a should be at least less than 0.04 to yield an accuracy loss within 5 %. When the truncation threshold $a = 0.04$, the probability of ΔS less than 5 % is 90.37 %, less than 10 % is 99.97 %, and less than 15 % is 100 %. Apparently, the probability curves are overly idealized, resulting in a slight overestimation of the probability of ΔS less than different limits when $a \leq 0.1$ ($b=98$).

From Fig. 12, the average truncation of earthquake records is about 54.60 % and 52.30 % (the maximum is 91.77 % and 90.89 %) under $D_{0.1-98 \%AI}$ and $D_{0.01-98 \%AI}$, respectively, and the average duration of the extracted seismic acceleration time windows is about 25.58 s and 26.97 s, respectively. Compared with the tail truncation of earthquake records, the leading truncation is relatively small and has little impact on improving computational efficiency of dynamic analyses. Therefore, conservatively, it is recommended not to trim the initial wave, and if necessary, the truncation threshold a be less than 0.01.

In summary, the dam response is more sensitive to the leading truncation (equivalently, the value of a) of an earthquake record than to the tail truncation (equivalently, the value of b). The main reasons can be explained from two aspects: 1) the asymmetry of seismic waveforms in the time series; 2) the cyclic hardening characteristic of rockfill

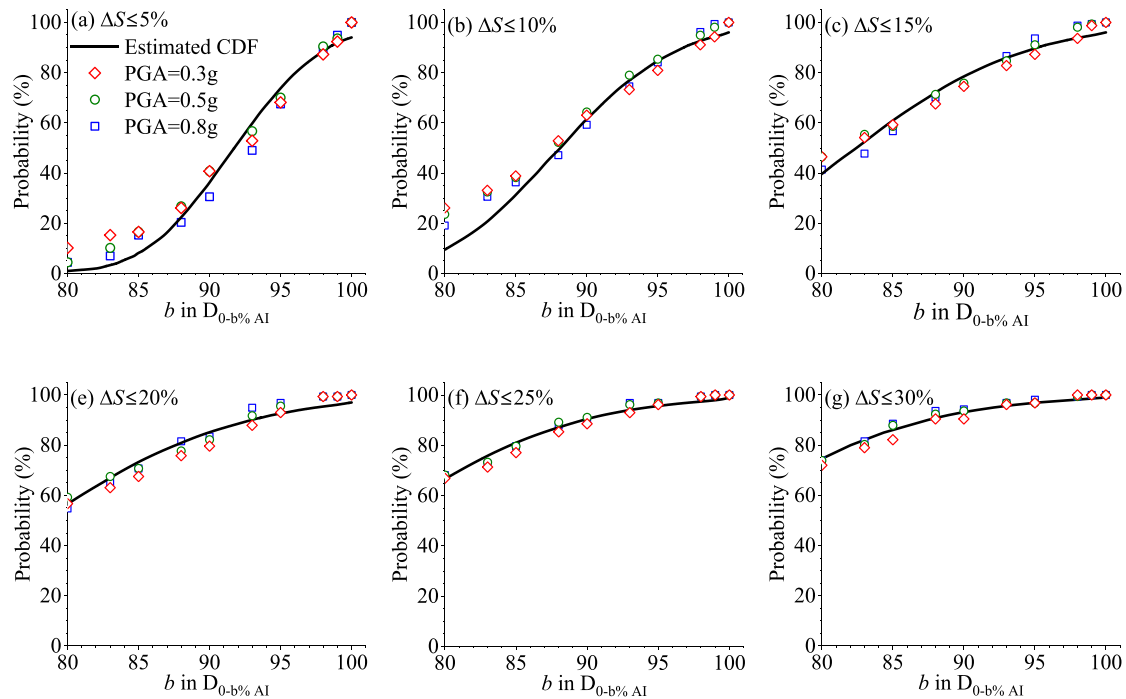


Fig. 8. Probability curves for ΔS less than different limits under $D_{0-b\%AI}$ (dot: counted fraction that ΔS is less than a given limit; black line: estimated lognormal distribution CDF).

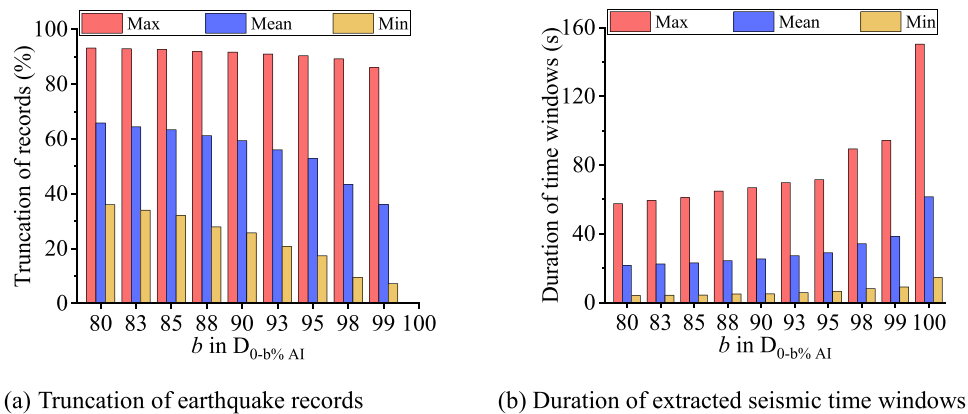


Fig. 9. Some statistics on earthquake record truncation under $D_{0-b\%AI}$ (PGA=0.3 g).

Table 2

Parameters θ and σ in Eq. (3) for ΔS less than different limits under $D_{0-b\%AI}$.

Parameters	$\Delta S \leq 5\%$	$\Delta S \leq 10\%$	$\Delta S \leq 15\%$	$\Delta S \leq 20\%$	$\Delta S \leq 25\%$	$\Delta S \leq 30\%$
θ	4.519	4.479	4.411	4.360	4.325	4.287
σ	0.055	0.074	0.113	0.134	0.134	0.143

materials under cyclic loading—the deformation rate after experiencing a large prior stress history will be significantly smaller than the initial loading[56,57].

6.3. Impact of record truncation on horizontal displacement of dam

Based on the analysis above, the damage potential of the seismic acceleration time windows extracted by $D_{0.01-98\%AI}$ has been evaluated in this section from the perspective of dam horizontal displacement. Table 4 presents the probabilities that the accuracy loss of maximum horizontal displacements of the benchmark dam is less than different

limits. It can be seen that the probability of the accuracy loss less than 5 % is 89.17 %, less than 10 % is 92.99 %, and less than 15 % is 94.90 %. It indicates that the seismic acceleration time windows extracted by $D_{0.01-98\%AI}$ effectively preserve the destructiveness of the original earthquake records.

6.4. Impact of record truncation on response spectra

To illustrate the extracted seismic acceleration time window, the truncation points of $a = 0.01$ and $b = 98$ are marked on the two earthquake records in Fig. 6 with dashed vertical lines. Meanwhile, Fig. 13

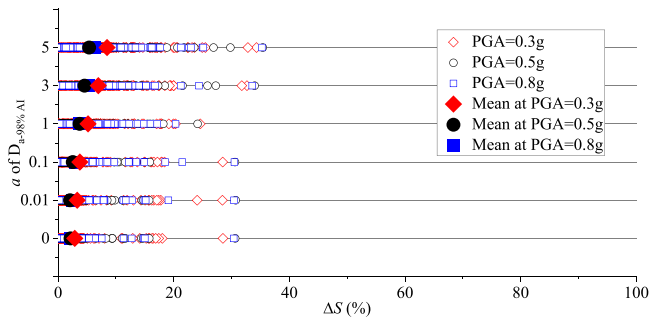


Fig. 10. $D_{a-98\%AI}$ - ΔS stripe plots.

compares the response spectra before and after truncating these two records by $D_{0.01-98\%AI}$. For comparison, these figures also provide the results when $a=5$ and $b=80$. It can be seen that when $a=5$ and $b=80$, the excessive truncation of earthquake records leads to a noticeable loss of response spectrum ordinates at the period greater than 1 s, especially the velocity and displacement response spectra, while the response spectrum ordinates under $D_{0.01-98\%AI}$ remain consistent with the original within the period of 0–4 s. It indicates it is feasible to work with the seismic time window under $D_{0.01-98\%AI}$ in dynamic analyses of high rockfill dams.

7. Conclusions

This paper aims to improve the computational efficiency of dynamic analyses for high rockfill dams by trimming the initial and coda waves of actual earthquake records. The significant duration definition is used as the truncation method for earthquake records, and the truncated seismic acceleration time windows are used as ground motion input. Based on 157 actual earthquake records, a large number of elastoplastic time-

history analyses on a 295m-high CRFD are conducted using the generalized plasticity model and seismic wave input method. The damage potential of the seismic acceleration time windows extracted by different truncation thresholds is quantified by establishing probability curves of dam response accuracy loss less than different limits. The optimal truncation metric is evaluated from crest settlement, dam horizontal displacement, and response spectra. The following conclusions are drawn:

- (1) The increase in peak ground acceleration (PGA) of input ground motions has a minimal impact on the probability curves of dam response accuracy loss for different truncation metrics.
- (2) Due to the asymmetry of seismic waveforms in time series and the cyclic hardening characteristic of rockfill materials, the tail of earthquake records is allowed to be truncated much more than the leading. The leading truncation threshold is suggested to be less than at least 0.01 % of Arias intensity.

Table 3

Parameters θ and σ in Eq. (2) for ΔS less than different limits under $D_{a-98\%AI}$.

Parameters	$\Delta S \leq 5\%$	$\Delta S \leq 10\%$	$\Delta S \leq 15\%$
θ	0.528	2.358	3.158
σ	2.876	1.617	1.369

Table 4

Probabilities for maximum horizontal displacement of the dam less than different limits under $D_{0.01-98\%AI}$.

Truncation metric	$\Delta S \leq 5\%$	$\Delta S \leq 10\%$	$\Delta S \leq 15\%$
$D_{0.01-98\%AI}$	89.17 %	92.99 %	94.90 %

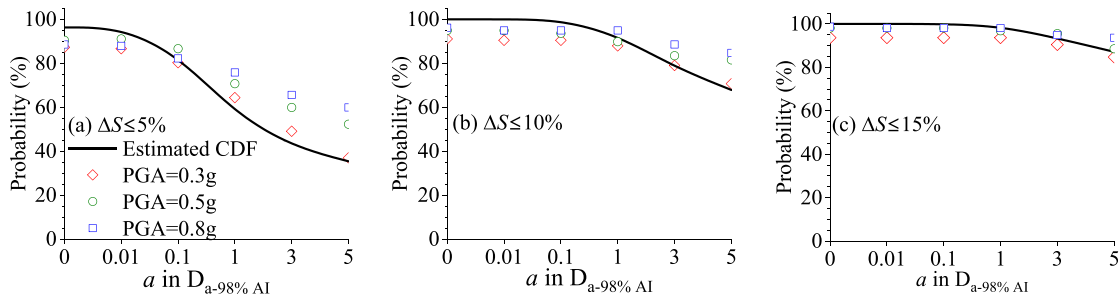


Fig. 11. Probability curves for ΔS less than different limits under $D_{a-98\%AI}$ (dot: counted fraction that ΔS is less than a given limit; black line: estimated lognormal distribution CDF).

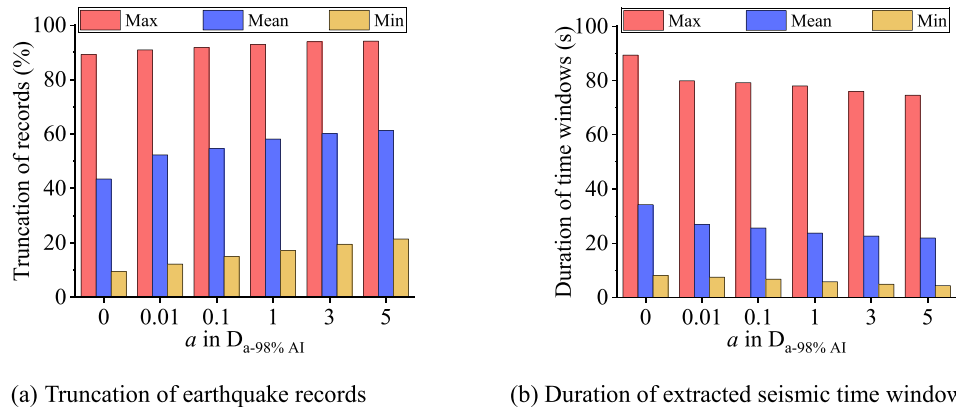


Fig. 12. Some statistics on earthquake record truncation under $D_{a-98\%AI}$ (PGA=0.3g).

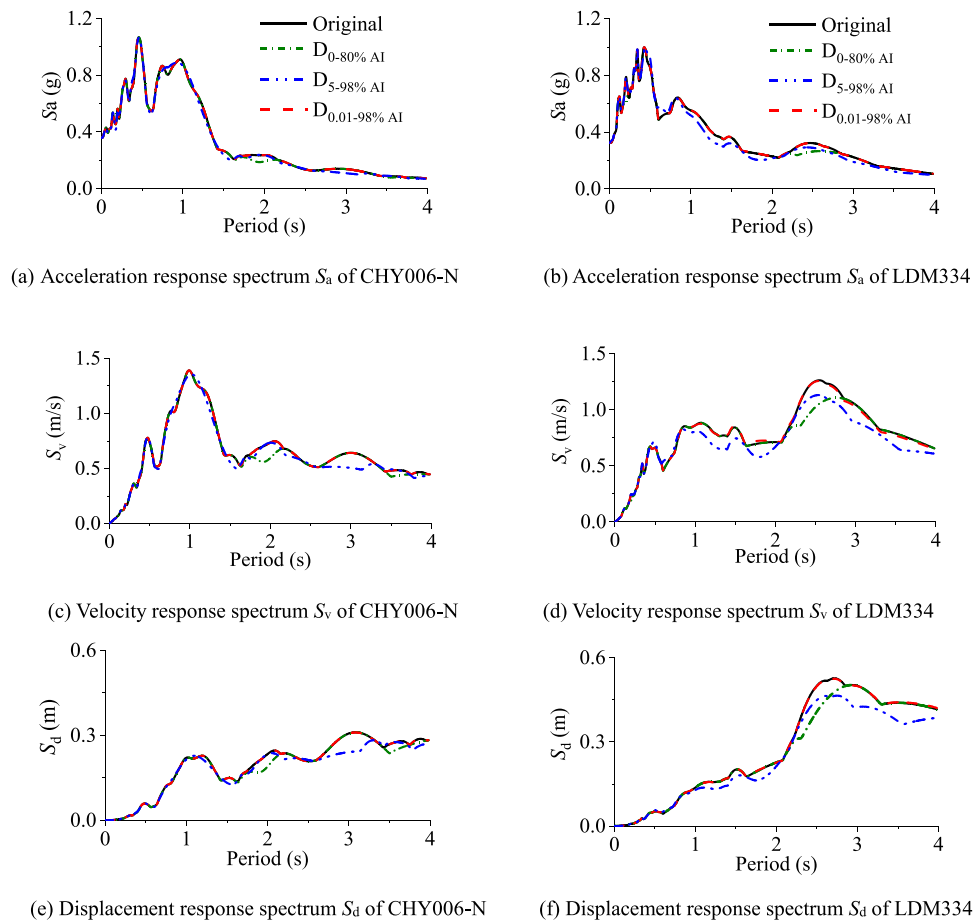


Fig. 13. Response spectra of the extracted seismic acceleration time windows under $D_{a-b\%AI}$.

- (3) The seismic time window constrained by 0.01–98 % Arias intensity is proved to be very effective and robust in accelerating nonlinear analyses of rockfill dams at an accuracy loss within 5 %, and the average reduction in computational workload reaches about 50 %. It is worth noting that the leading truncation of earthquake records is extremely small compared with the tail truncation and contributes little to the reduction in computational workload.
- (4) It is essential to employ a quantitative approach to estimate the truncation points of earthquake records from a statistical perspective, as relying on visual inspection of the records may lead to inaccurate and misleading conclusions. Excessive truncation thresholds lead to the severe loss of time and frequency domains information of earthquake records, resulting in seismic signal distortion and damage potential loss.

The conclusions are highly applicable to the works with high timeliness and large sample capacity, such as post-earthquake rapid emergency assessment, incremental dynamic analysis, and machine learning.

CRediT authorship contribution statement

Degao Zou: Supervision, Software, Project administration, Funding

acquisition, Conceptualization. **Qitong Jiang:** Writing – original draft, Visualization, Validation, Resources, Methodology, Investigation, Formal analysis, Data curation. **Chenguang Zhou:** Writing – review & editing, Validation, Software, Funding acquisition. **Kai Chen:** Software, Methodology. **Yongqian Qu:** Writing – review & editing, Formal analysis. **Jingmao Liu:** Writing – review & editing, Supervision, Software, Project administration, Funding acquisition, Formal analysis. **Duo Li:** Writing – review & editing.

Declaration of Competing Interest

The authors declare that they have no known competing financial interests or personal relationships that could have appeared to influence the work reported in this paper.

Acknowledgements

This work was supported by the National Natural Science Foundation of China (Grant Nos. 52192674, 52079023, U2240211) and Major Science & Technology Project of the Ministry of Water Resources of China (No. SKS-2022101).

Appendix A

Table A.1

Actual earthquake records used in present paper.

Earthquake Name	Year	Magnitude	Record name
Chi-Chi_Taiwan	1999	7.62	CHY006-N, CHY006-V, CHY010-W, CHY014-N, CHY024-E, CHY028-V, CHY029-E, CHY074-E, CHY086-N, CHY088-N, CHY101-E, TCU034-E, TCU042-E, TCU042-N, TCU047-V, TCU049-E, TCU053-E, TCU055-E, TCU060-E, TCU065-V, TCU067-E, TCU067-N, TCU067-V, TCU068-E, TCU068-V, TCU071-E, TCU072-V, TCU075-E, TCU075-V, TCU076-E, TCU076-N, TCU076-V, TCU078-E, TCU078-N, TCU079-E, TCU082-E, TCU084-N, TCU084-V, TCU089-E, TCU089-N, TCU095-V, TCU122-E, TCU122-N, TCU122-V, TCU138-W
Coalinga-01	1983	6.36	H-CAK270, H-Z14090, H-PV1090, H-PVB045
Dinar_Turkey	1995	6.40	DIN090, DIN180
ImperialValley-02	1940	6.95	I-ELC180
ImperialValley-06	1979	6.53	H-CHI012, H-DLT262, H-DLT352
Kobe_Japan	1995	6.90	ABN000, ABN090, AMA-UP, AMA000, KJM-UP, KAK000, KAK090, KBU-UP, KBU090, NIS-UP, NIS000, NIS090, TDO000, TAZ-UP, TAK-UP
Kocaeli_Turkey	1999	7.51	ATS000, ARE000, DZC-UP, DZC180, DZC270, GBZ000, IZT090, YPT-UP
Kozani_Greece-01	1995	6.40	KOZ-L
Kozani_Greece-04	1995	5.10	C-KRP-NS
LomaPrieta	1989	6.93	G01090, A01000, PAE055, PAE325, LEX000, LEX090
Manjil_Iran	1990	7.37	ABBAR-T, ABBAR-V, ABBAR-V_1
N.PalmSprings	1986	6.06	DSP000
NorthernCalif-07	1975	5.20	D-CPM120
Northridge-01	1994	6.69	GR2180, VRM-UP, STN020, STN110, SPV-UP, UCL-UP, UCL090, UCL360, UNI005, UNI095, LA0180, LA0180_1, LA0270, LDM-UP, LDM064, LDM334, NYA090, BRC090, H12180, H12180_1, L09090, MRP180, MTW000, CWC-UP, CWC180, CWC270, NWH-UP, WPI-UP, WPI316, STC090, STC180, SUN190, PAC175, PAC265, PKC090, PKC360, PAR-UP, SMV180, PTM090, RRS318, GRN270, STM-UP, STM360, SSU000, SSU090, KAT-UP, KAT090, RO3-UP, RO3000, RO3090, GLE-UP, SCE-UP, SCE281, SYL-UP, TPF270
NorthwestChina-03	1997	6.10	JIA270
SanFernando	1971	6.61	PSL270, ORR291, PEL090
SuperstitionHills-02	1987	6.54	B-ICC000, B-ICC090, B-WSM180, B-IVW360
Westmorland	1981	5.90	WSM090
Darfield_New Zealand	2010	7.00	LPCCN80E, LPCCS10E

Appendix B

In generalized plasticity model, the relationship between incremental stress and strain is

$$d\sigma = D^e d\epsilon \quad (B.1)$$

in which the incremental strain is comprised of incremental elastic strain and plastic strain, as follows:

$$d\epsilon = d\epsilon^e + d\epsilon^p \quad (B.2)$$

And the elasto-plastic stiffness tensor is expressed as:

$$D^e = D^e - \frac{D^e \mathbf{n}_g \mathbf{n}^T D^e}{H_{L/U} + \mathbf{n}^T D^e \mathbf{n}_g} \quad (B.3)$$

where D^e is the elastic stiffness tensor; \mathbf{n} is the loading direction vector; H is the plastic modulus; \mathbf{n}_g is the plastic flow direction vector. And loading and unloading are denoted by the subscripts L and U, respectively.

The loading and unloading criteria are expressed as

$$\begin{aligned} \mathbf{n}^T d\sigma^e &> 0 \text{ (Loading)} \\ \mathbf{n}^T d\sigma^e &= 0 \text{ (Neutral loading)} \\ \mathbf{n}^T d\sigma^e &< 0 \text{ (Unloading)} \end{aligned} \quad (B.4)$$

The elastic shear and bulk moduli are expressed as

$$G = G_0 p_a \left(\frac{p}{p_a} \right)^{m_s} \quad (B.5)$$

$$K = K_0 p_a \left(\frac{p}{p_a} \right)^{m_v} \quad (B.6)$$

where G_0 , K_0 , m_s , m_v are model constants; p_a is one atmospheric pressure; p is the mean effective stress.

The plastic flow direction vector is expressed as:

$$\mathbf{n}_g^T = \left(\frac{d_g}{\sqrt{1+d_g^2}}, \frac{1}{\sqrt{1+d_g^2}} \right) \quad (\text{B.7})$$

in which $d_g = (1 + \alpha_g)(M_g - \eta)$; $\eta = q/p$ is the stress ratio; $M_g = 6 \sin \phi'_g / (3 - \sin \phi'_g \sin 3\theta)$; ϕ'_g is the angle of internal friction at the critical state; θ is the stress Lode's angle; α_g is a model constant.

And the loading direction vector is expressed as

$$\mathbf{n}^T = \left(\frac{d_f}{\sqrt{1+d_f^2}}, \frac{1}{\sqrt{1+d_f^2}} \right) \quad (\text{B.8})$$

in which $d_f = (1 + \alpha_f)(M_f - \eta)$; α_f and M_f are model constants.

The plastic moduli of loading/reloading and unloading are respectively expressed as

$$H_L = H_0 p_a \left(\frac{p}{p_a} \right)^{m_l} \left[1 - \frac{\eta}{(1 + 1/\alpha_f) M_f} \right]^4 \left[1 - \frac{\eta}{M_g} + \beta_0 \beta_1 \exp(-\beta_0 \xi) \right] H_{DM} H_{den} \quad (\text{B.9})$$

$$H_u = H_{u0} p_a \left(\frac{p}{p_a} \right)^{m_u} \left(\frac{\eta_u}{M_g} \right)^{-\gamma_u} H_{den} \quad |\eta_u/M_g| < 1 \quad (\text{B.10})$$

where $\xi = \int |d\epsilon_s^q|$ is the accumulative plastic shear strain; $H_{den} = \exp(-\gamma_d \epsilon_v)$ is the densification coefficient; ϵ_v is the volumetric strain; $H_{DM} = \exp(-\eta/\eta_{max})^{\gamma_{DM}}$ is the stress history function; η_{max} is the largest value of the stress ratio ever reached. $\beta_0, \beta_1, H_0, H_{u0}, \gamma_d, \gamma_u, \gamma_{DM}, m_l, m_u$ are model constants.

References

- [1] Karalar M, Cavusli M. Assessing 3D seismic damage performance of a CFR dam considering various reservoir heights. *Earthq Struct* 2019;16(2):221–34.
- [2] Karalar M, Cavusli M. Examination of 3D long-term viscoplastic behaviour of a CFR dam using special material models. *Geomech Eng* 2019;17(2):119–31.
- [3] Karalar M, Çavuşlu M. Evaluation of 3D nonlinear earthquake behaviour of the ilisu CFR dam under far-fault ground motions. *Adv Civ Eng* 2019;2019(1):7358710.
- [4] Karalar M, Cavusli M. Seismic effects of epicenter distance of earthquake on 3D damage performance of CG dams. *Earthq Struct* 2020;18(2):201–13.
- [5] Karalar M, Cavusli M. Three dimensional seismic deformation-shear strain-swelling performance of America-California Oroville Earth-Fill Dam. *Geomech Eng* 2021;24(5):443–56.
- [6] Karalar M, Cavusli M. Determination of 3D near fault seismic behaviour of Oroville earth fill dam using burger material model and free field-quiet boundary conditions. *Math Comput Model Dyn Syst* 2022;28(1):55–77.
- [7] Li S, He Y, Wei Y. Truncation method of ground motion records based on the equivalence of structural maximum displacement responses. *J Earthq Eng* 2022;26(10):5268–89.
- [8] Zakian P, Kaveh A. Seismic design optimization of engineering structures: a comprehensive review. *Acta Mech* 2023;234(4):1305–30.
- [9] He Y, Zhao J, Yao L, et al. A deep learning-based ground motion truncation method to improve efficiency of structural time history analysis. *Structures*, 63. Elsevier; 2024.
- [10] Aki Keiiti. Analysis of the seismic coda of local earthquakes as scattered waves. *J Geophys Res* 1969;74(2):615–31. <https://doi.org/10.1029/JB074i002p00615>.
- [11] Aki K, Chouet B. Origin of coda waves: source, attenuation, and scattering effects. *J Geophys Res* 1975;80(23):3322–42.
- [12] Trifunac MD, Brady AG. A study on the duration of strong earthquake ground motion. *Bull Seismol Soc Am* 1975;65(3):581–626.
- [13] Widmer-Schmidrig R. What can superconducting gravimeters contribute to normal-mode seismology? *Bull Seismol Soc Am* 2003;93(3):1370–80.
- [14] Bommer JJ, Martínez-Pereira A. The effective duration of earthquake strong motion. *J Earthq Eng* 1999;3(02):127–72.
- [15] Ruiz-Garcia J. On the influence of strong-ground motion duration on residual displacement demands. *Earthq Struct* 2010;1(4):327–44.
- [16] Samanta A, Megawati K, Pan T. Duration-dependent inelastic response spectra and effect of ground motion duration[C]//Proc., 15th World Conf. on Earthquake Engineering, Lisbon, Portugal. 2012.
- [17] Ou Y, Song J, Wang P, et al. Ground motion duration effects on hysteretic behavior of reinforced concrete bridge columns. *J Struct Eng* 2014;140(3):04013065.
- [18] Sun P, Huang D, Du S. Improving soil liquefaction prediction through an extensive database and innovative ground motion characterization: a case study of Port Island liquefied site. *Soil Dyn Earthq Eng* 2023;165:107696.
- [19] Hou H, Qu B. Duration effect of spectrally matched ground motions on seismic demands of elastic perfectly plastic SDOFS[J]. *Eng Struct* 2015;90:48–60.
- [20] Khaloo A, Nozhati S, Masoomi H, et al. Influence of earthquake record truncation on fragility curves of RC frames with different damage indices. *J Build Eng* 2016;7:23–30.
- [21] Somerville PG, Smith NF, Graves RW, Abrahamson NA. Modification of empirical strong ground motion attenuation relations to include the amplitude and duration effects of rupture directivity. *Seismol Res Lett* 1997;68(1):199–222.
- [22] Repapis CC, Mimoglou PP, Dimakopoulou VV, et al. Efficient strong motion duration of pulse-like records for nonlinear structural analyses. *Earthq Eng Struct Dyn* 2020;49(5):479–97.
- [23] Dimakopoulou V, Fragiadakis M, Taflampas I. A wavelet-based approach for truncating pulse-like records. *Bull Earthq Eng* 2022;1–24.
- [24] Jin A, Pan J, Wang J, et al. A spectrum-based earthquake record truncation method for nonlinear dynamic analysis of arch dams. *Soil Dyn Earthq Eng* 2020;132:106104.
- [25] Reyes JC, Avila WA, Kalkan E, et al. Reducing processing time of nonlinear analysis of symmetric-plan buildings. *J Struct Eng* 2021;147(6):04021073.
- [26] Baker J.W. Vector-valued ground motion intensity measures for probabilistic seismic demand analysis[M]. Stanford University, 2005.
- [27] Pan J, Xu Y, Jin F. Seismic performance assessment of arch dams using incremental nonlinear dynamic analysis. *Eur J Environ Civ Eng* 2015;19(3):305–26.
- [28] Pang R, Xu B, Kong X, et al. Seismic fragility for high CFRDs based on deformation and damage index through incremental dynamic analysis. *Soil Dyn Earthq Eng* 2018;104:432–6.
- [29] Kong X, Zhou C, Zou D. Influence of the dynamic interaction between high rockfill dam and foundation. *J Hydraul Eng* 2019;50(12):1417–32 ([In Chinese]).
- [30] Ooi ET, Man H, Natarajan S, et al. Adaptation of quadtree meshes in the scaled boundary finite element method for crack propagation modelling. *Eng Fract Mech* 2015;144:101–17.
- [31] Wolf JP, Schanz M. The scaled boundary finite element method. *Comput Mech* 2004;33(4): 326–326.
- [32] Song C. The scaled boundary finite element method: introduction to theory and implementation. John Wiley & Sons; 2018.
- [33] NB/T 11559.2-2024. Guidelines for finite element analysis for hydropower projects. Proofed.; 2024.
- [34] Westergaard HM. Water pressures on dams during earthquakes. *Trans Asce* 1933; 98(2):418–32.
- [35] Zou D., Kong X., Xu B. User Manual for Geotechnical Dynamic Nonlinear Analysis, 2005.
- [36] Xu B, Zou D, Liu H. Three-dimensional simulation of the construction process of the Zipingpu concrete face rockfill dam based on a generalized plasticity model. *Comput Geotech* 2012;43:143–54.
- [37] Zou D, Xu B, Kong X, et al. Numerical simulation of the seismic response of the Zipingpu concrete face rockfill dam during the Wenchuan earthquake based on a generalized plasticity model. *Comput Geotech* 2013;49:111–22.
- [38] Ancheta TD, Darragh RB, Stewart JP, Seyhan E, Silva WJ, Chiou BSJ, et al. NGA-West2 database. *Earthq Spectra* 2014;30(3):989–1005.
- [39] Xu Y, Lu X, Tian Y, et al. Real-time seismic damage prediction and comparison of various ground motion intensity measures based on machine learning. *J Earthq Eng* 2022;26(8):4259–79.
- [40] Ozkan MY. A review of considerations on seismic safety of embankments and earth and rock-fill dams. *Soil Dyn Earthq Eng* 1998;17(7-8):439–58.

- [41] Han B, Zdravkovic L, Kontoe S, et al. Numerical investigation of the response of the Yele rockfill dam during the 2008 Wenchuan Earthquake. *Soil Dyn Earthq Eng* 2016;88:124–42.
- [42] Kalkan Y, Potts LV, Bilgi S. Assessment of vertical deformation of the ataturk dam using geodetic observations[J]. *J Surv Eng* 2016;142(2):04015011.
- [43] Marin A, Laue J. Displacement-based seismic analysis of slopes, dams and embankments. *J Earthq Tsunami* 2016:181–213.
- [44] Huang Y, Xiong M. Probability density evolution method for seismic liquefaction performance analysis of earth dam. *Earthq Eng Struct Dyn* 2016;46(6):925–43.
- [45] Pang R, Xu B, et al. Stochastic seismic performance assessment of high CFRDs based on generalized probability density evolution method. *Comput Geotech* 2018.
- [46] Liu J, Lu Y. A direct method for analysis of dynamic soil-structure interaction based on interface idea[M]//Developments. geotechnical engineering, 83. Elsevier;; 1998. p. 261–76.
- [47] Pan J, Zhang C, Wang J, et al. Seismic damage-cracking analysis of arch dams using different earthquake input mechanisms. *Sci China Ser E: Technol Sci* 2009;52(2): 518–29.
- [48] Tarinejad R, Fatehi R, Harichandran RS. Response of an arch dam to non-uniform excitation generated by a seismic wave scattering model. *Soil Dyn Earthq Eng* 2013;52:40–54.
- [49] Clough R.W. Nonlinear mechanisms in the seismic response of arch dams[C]// International research conference on earthquake engineering, Skopje, Yugoslavia, 1980.
- [50] Gao Y, Zhang N. Scattering of cylindrical SH waves induced by a symmetrical V-shaped canyon: near-source topographic effects. *Geophys J Int* 2013;193(2): 874–85.
- [51] Du X, Zhao M, Wang J. A stress artificial boundary in FEA for near-field wave problem. *Acta Mechanica Sin-Chin Ed* 2006;38(1):49.
- [52] Huang J, Zhao M, Du X. Non-linear seismic responses of tunnels within normal fault ground under obliquely incident P waves. *Tunn Undergr Space Technol* 2017; 61:26–39.
- [53] Gao Z, Zhao X, Zhao M, et al. Efficient seismic analysis for nonlinear soil-structure interaction with a thick soil layer. *Earthq Eng Eng Vib* 2021;20:553–65.
- [54] Smith WD. The application of finite element analysis to body wave propagation problems. *Geophys J Int* 1975;42(2):747–68.
- [55] Swaisgood J.R. Embankment dam deformations caused by earthquakes[C]//Pacific conference on earthquake engineering. 2003, 14.
- [56] Liu H, Zou D, Liu J. Constitutive modeling of dense gravelly soils subjected to cyclic loading. *Int J Numer Anal Methods Geomech* 2014;38(14):1503–18.
- [57] Xia P, Zeng C, Shao L, et al. Axial strain accumulation projection model for sand in cyclic loading. *Soil Dyn Earthq Eng* 2021;147:106819.